Mon. Not. R. Astron. Soc. **000**, 000–000 (0000) Printed 12 February 2013 (MN LaTeX style file v2.2)

Baryon Census in Hydrodynamical Simulations of Galaxy Clusters

S. Planelles[1,2]⋆ , S. Borgani[1,2,3], K. Dolag[4,5], S. Ettori[6], D. Fabjan[3,7,8], G. Murante[2], L. Tornatore[1]

[1] *Astronomy Unit, Department of Physics, University of Trieste, via Tiepolo 11, I-34131 Trieste, Italy*
[2] *INAF, Osservatorio Astronomico di Trieste, via Tiepolo 11, I-34131 Trieste, Italy*
[3] *INFN – National Institute for Nuclear Physics, Trieste,Italy*
[4] *Universitätssternwarte München, München, Germany*
[5] *Max-Planck-Institut für Astrophysik, Garching, Germany*
[6] *INAF, Osservatorio Astronomico di Bologna, via Ranzani 1, I-40127 Bologna, Italy*
[7] *SPACE-SI, Slovenian Centre of Excellence for Space Sciences and Technologies, Aškerčeva 12, 1000 Ljubljana, Slovenia*
[8] *Faculty of Mathematics and Physics, University of Ljubljana, Jadranska 19, 1000 Ljubljana, Slovenia*

12 February 2013

ABSTRACT

We carry out an analysis of a set of cosmological SPH hydrodynamical simulations of galaxy clusters and groups aimed at studying the total baryon budget in clusters, and how this budget is shared between the hot diffuse component and the stellar component. Using the TreePM+SPH `GADGET-3` code, we carried out one set of non–radiative simulations, and two sets of simulations including radiative cooling, star formation and feedback from supernovae (SN), one of which also accounting for the effect of feedback from active galactic nuclei (AGN). The analysis is carried out with the twofold aim of studying the implication of stellar and hot gas content on the relative role played by SN and AGN feedback, and to calibrate the cluster baryon fraction and its evolution as a cosmological tool. With respect to previous similar analysis, the simulations used in this study provide us with a sufficient statistics of massive objects and including an efficient AGN feedback. We find that both radiative simulation sets predict a trend of stellar mass fraction with cluster mass that tends to be weaker than the observed one. However this tension depends on the particular set of observational data considered. Including the effect of AGN feedback alleviates this tension on the stellar mass and predicts values of the hot gas mass fraction and total baryon fraction to be in closer agreement with observational results. We further compute the ratio between the cluster baryon content and the cosmic baryon fraction, Y_b, as a function of cluster-centric radius and redshift. At R_{500} we find for massive clusters with $M_{500} > 2\times10^{14}\,h^{-1}M_\odot$ that Y_b is nearly independent of the physical processes included and characterized by a negligible redshift evolution: $Y_{b,500} = 0.85 \pm 0.03$ with the error accounting for the intrinsic r.m.s. scatter within the set of simulated clusters. At smaller radii, R_{2500}, the typical value of Y_b slightly decreases, by an amount that depends on the physics included in the simulations, while its scatter increases by about a factor of two. These results have interesting implications for the cosmological applications of the baryon fraction in clusters.

Key words: cosmology: miscellaneous – methods: numerical – galaxies: cluster: general – X-ray: galaxies.

1 INTRODUCTION

Galaxy clusters, which stem from the collapse of density fluctuations involving comoving scales of tens of Mpc, are the largest gravitationally bound structures in the Universe. Since they are relatively well isolated systems, knowledge of their baryon content is a key ingredient to understand the physics of these objects and their use as cosmological probes (see Allen et al. 2011; Kravtsov and Borgani 2012, for recent reviews). The most massive galaxy clusters are of particular cosmological interest since their baryon content is expected to trace accurately the baryon content of the Universe. In the absence of dissipation, the ratio of baryonic-to-total mass in clusters should closely match the ratio of the cosmological parameters measured from the cosmic microwave back-

⋆ e-mail: susana.planelles@oats.inaf.it

ground (CMB) and, therefore, $M_b/M_{tot} \sim \Omega_b/\Omega_m$ (White et al. 1993; Evrard 1997; Ettori et al. 2003; Allen et al. 2008).

However, contrary to expectations, measurements of the baryon mass fraction in nearby clusters from optical and X-ray observations have posed a challenge to this fundamental assumption since they have reported smaller values than expected (e.g., Ettori et al. 2003; Biviano and Salucci 2006; McCarthy et al. 2007) together with a possible intriguing trend with cluster mass (e.g., Lin et al. 2003, 2012) for a broad mass range of systems. With the precise measurement of the universal baryon fraction, $f_b \equiv \Omega_b/\Omega_m = 0.167 \pm 0.004$, from the *Wilkinson Microwave Anisotropy Probe* (WMAP-7; Komatsu et al. 2011), these discrepancies have gained in physical importance and claim for different explanations: physical processes which lower $f_{\rm b}$ in clusters relative to the universal fraction (see e.g., Bialek et al. 2001; He et al. 2006), significant undetected baryon components by standard X-ray and/or optical techniques (see Ettori et al. 2003; Lin and Mohr 2004), or a systematic underestimate of $\Omega_{\rm m}$ by WMAP (McCarthy et al. 2007).

In this sense, the correct determination of the gas mass fraction may be crucial. In fact, studies of the individual baryon components have shown that the stellar and gas mass fractions within R_{500}[1] exhibit opposite behaviours as a function of the total system mass. In particular, clusters have a higher gas mass fraction than groups (e.g., Vikhlinin et al. 2006; Arnaud et al. 2007), but a lower stellar mass fraction (Lin et al. 2003). This has been interpreted as a difference in the star formation efficiency between groups and clusters (e.g., David et al. 1990; Lin et al. 2003; Laganá et al. 2008).

On the other hand, the mass dependence of the gas fraction and the discrepancy between the baryon mass fraction in groups/clusters and the WMAP value can be understood in terms of non–gravitational processes. In this regard, AGN heating, which can drive the gas outside the potential wells of host halos, can explain the lack of gas within R_{500} in groups. Therefore, groups also appear as critical systems to assess the universality of the baryon fraction and to understand complex physical processes affecting both the gas and the stellar components.

The baryonic mass content of clusters consists of stars in cluster galaxies (satellite galaxies plus the brightest cluster galaxy or BCG), intra-cluster light (ICL, stars that are not bound to cluster galaxies), and the hot intra-cluster medium (ICM) whose mass exceeds the mass of the former two stellar components by a factor of ~ 6. Therefore, to reliably estimate the cosmological parameters from the baryonic-to-total mass ratio one should address all the baryonic components and not only the gas mass. In fact, to explain the discrepancy between the observed baryon fraction and the cosmic value, the ICL is suggested to be one of the most important forms of missing baryons, accounting for $6-22$ per cent of the total cluster light in the r–band (e.g., Gonzalez et al. 2007), or even more in cluster mergers (e.g., Pierini et al. 2008). Cosmological simulations report that the ICL accounts for up to $\simeq 60$ per cent of the total of stars (e.g., Murante et al. 2004, 2007; Puchwein et al. 2010). However, although this large fraction of ICL is sufficient to explain the discrepancy with the cosmic value, it seems to be in contradiction with observations. On one hand, this suggests that other mechanisms, like gas expulsion by AGN heating, may also be important to account for the missing baryons. On the other hand, one should also bear in mind that the methods to identify ICL in simulations and in observations are quite different, the former being often based on criteria of gravitational boundness of star particles, while the latter being based on criteria of surface brightness limits (e.g. Rudick et al. 2006).

The combination of robust measurements of the baryonic mass fraction in clusters from X-ray observations together with a determination of $\Omega_{\rm b}$ from CMB data or big-bang nucleosynthesis calculations and a constraint on the Hubble constant, can therefore be used to measure $\Omega_{\rm m}$ (e.g., White and Frenk 1991; White et al. 1993; Evrard 1997; Allen et al. 2002; Ettori et al. 2003; Lin et al. 2003; Allen et al. 2003, 2004, 2008). This method, remarkably simple and robust in terms of its underlying assumptions, currently provides strong constraints on $\Omega_{\rm m}$. On the other hand, measurements of the apparent redshift evolution of the cluster X-ray gas mass fraction, hereafter f_g, can also be used to constrain the geometry of the Universe (Sasaki 1996), its acceleration (Pen 1997) and, therefore, the dark energy equation of state (e.g., Ettori et al. 2003, 2009; Allen et al. 2002, 2003, 2004; LaRoque et al. 2006; Allen et al. 2008, 2011). This diagnostic exploits the dependence of the f_g measurements (derived from the observed X-ray gas temperature and density profiles) on the assumed distances to the clusters, $f_{\rm g} \propto d^{1.5}$, and relies on cluster baryon fractions being roughly universal and non-evolving over the redshift range where they can be observed (typically $z < 1$). Therefore, like Type Ia supernovae, massive clusters serve as standard calibration sources that test the expansion history of the universe.

In this regard, early simulations by Eke et al. (1998) have been used to calibrate the depletion factor, i.e., the ratio by which the baryon fraction measured at R_{2500} is depleted with respect to the universal mean (see, for instance, Allen et al. 2008). These non-radiative simulations indicate that, within the virial radius, the baryon fraction in clusters provides a measure of the universal mean that is only slightly biased low by ~ 10 per cent. The magnitude of this bias might change if additional physics is included in the simulations. Therefore, it is necessary and extremely useful to deepen in the analysis of how different implementations of baryonic physics can affect the value of this bias, its evolution with redshift, its radial dependence within clusters, or some statistics with massive galaxy clusters.

Using non-radiative hydrodynamical simulations the expectation is that, for the largest ($kT > 5\,$keV), dynamically relaxed clusters and for measurement radii beyond the innermost core ($r > R_{2500}$), f_g should be approximately constant with redshift (e.g., Eke et al. 1998; Crain et al. 2007). However, possible systematic variations of f_g with redshift can be accounted for in a straightforward manner if the allowed range of such variations is constrained by numerical simulations or other complementary data (Eke et al. 1998; Bialek et al. 2001; Muanwong et al. 2002; Borgani et al. 2004; Kay et al. 2004; Ettori et al. 2004, 2006; Kravtsov et al. 2005; Nagai et al. 2007).

Therefore, it is clear that understanding the baryon mass fraction and its mass and redshift dependence is a crucial issue to understand better astrophysics in galaxy clusters, e.g., the origin of the ICL (e.g., Pierini et al. 2008), star-formation history (e.g., Fritz et al. 2011), metal-enrichment history (e.g., Kapferer et al. 2009), the dynamical history of galaxy clusters, and the use of these systems to constrain the cosmological parameters (e.g., Allen et al. 2011).

The purpose of the present work is to use a set of hydrodynamical simulations of galaxy clusters, characterized by different physical processes, to study how the fraction and spatial distribu-

[1] R_Δ (Δ=2500, 500, 200) is the radius within which the mass density of a group/cluster is equal to Δ times the critical density (ρ_c) of the Universe. Correspondingly, $M_\Delta = \Delta\, \rho_c(z)\, (4\,\pi/3) R_\Delta^3$ is the mass inside R_Δ.

tion of baryons, as contributed both by the stellar component and by the hot X-ray emitting gas, are affected by the physical conditions within clusters and how these results compare with observations. We also analyse how the different baryonic depletions depend on redshift, baryonic physics, and cluster radius, determining, therefore, some implications for the constraints on cosmological parameters derived from gas mass fractions within clusters. In this regard, our analysis extends previous analyses of the baryon fraction in cluster simulations which included only non–radiative physics (e.g., Evrard 1990; Metzler and Evrard 1994; Navarro et al. 1995; Lubin et al. 1996; Eke et al. 1998; Frenk et al. 1999; Mohr et al. 1999; Bialek et al. 2001), the processes of cooling and star formation (e.g., Muanwong et al. 2002; Kay et al. 2004; Ettori et al. 2004; Kravtsov et al. 2005; Ettori et al. 2006; De Boni et al. 2011; Sembolini et al. 2012), and the effect of AGN feedback (e.g., Puchwein et al. 2008, 2010; Fabjan et al. 2010; Young et al. 2011; Battaglia et al. 2012). In addition, with respect to previous similar analysis, the simulations presented in this work provide us with a sufficient statistics of massive objects and including an efficient AGN feedback.

The paper is organized as follows: in Section 2, we describe our dataset of simulated galaxy clusters and the different physical processes considered in re-simulating them; in Section 3, we present the results obtained from this set of simulations on the baryon, gas and stellar mass fractions as a function of cluster mass and we compare these results with different observational data sets; in Section 4 we calibrate the different baryonic depletions and analyse their dependences on redshift, baryonic physics and cluster radius; and finally, in Section 5, we summarize and discuss our findings.

2 THE SIMULATED CLUSTERS

2.1 Initial conditions

Our sample of simulated clusters and groups are obtained from 29 Lagrangian regions, centred around as many massive halos identified within a large-volume, low-resolution N-body cosmological simulation (see Bonafede et al. 2011, for details). The parent Dark Matter (DM) simulation followed 1024^3 DM particles within a box having a comoving side of 1 h^{-1} Gpc, with h the Hubble constant in units of 100 km s^{-1} Mpc^{-1}. The cosmological model assumed is a flat ΛCDM one, with $\Omega_{\rm m} = 0.24$ for the matter density parameter, $\Omega_{\rm b} = 0.04$ for the contribution of baryons, $H_0 = 72$ km s^{-1} Mpc^{-1} for the present-day Hubble constant, $n_{\rm s} = 0.96$ for the primordial spectral index and $\sigma_8 = 0.8$ for the normalisation of the power spectrum. Within each Lagrangian region we increased the mass resolution and added the relevant high-frequency modes of the power spectrum, following the zoomed initial condition (ZIC) technique (Tormen et al. 1997). Outside these regions, particles of mass increasing with distance from the target halo are used, so as to keep a correct description of the large scale tidal field. Each high-resolution Lagrangian region is shaped in such a way that no low-resolution particle contaminates the central halo at $z = 0$ at least out to 5 virial radii[2]. As a result, each region is sufficiently large to contain more than one interesting halo with no contaminants within its virial radius.

[2] The virial radius, R_{vir}, is defined as the radius encompassing the overdensity of virialization, as predicted by the spherical collapse model (e.g., Eke et al. 1996).

Initial conditions have been generated by adding a gas component only in the high–resolution region, by splitting each particle into two, one representing DM and another representing the gas component, with a mass ratio such to reproduce the cosmic baryon fraction. The mass of each DM particle is $m_{\rm DM} = 8.47 \cdot 10^8\ h^{-1} M_\odot$ and the initial mass of each gas particle is $m_{\rm gas} = 1.53 \cdot 10^8\ h^{-1} M_\odot$.

2.2 The simulation models

All the simulations have been carried out with the TreePM–SPH GADGET-3 code, a more efficient version of the previous GADGET-2 code (Springel 2005). In the high–resolution region gravitational force is computed by adopting a Plummer-equivalent softening length of $\epsilon = 5\,{\rm h}^{-1}$ kpc in physical units below $z = 2$, while being kept fixed in comoving units at higher redshift (see Borgani et al. 2006, for an analysis of the effect of softening on radiative simulations of galaxy clusters). As for the hydrodynamic forces, we assume the minimum value attainable by the SPH smoothing length of the B–spline kernel to be half of the corresponding value of the gravitational softening length.

Besides a set of non–radiative hydrodynamic simulations (`NR` hereafter), we carried out two sets of radiative simulations.

Radiative cooling rates are computed by following the same procedure presented by Wiersma et al. (2009). We account for the presence of the cosmic microwave background (CMB) and of UV/X–ray background radiation from quasars and galaxies, as computed by Haardt and Madau (2001). The contributions to cooling from each one of eleven elements (H, He, C, N, O, Ne, Mg, Si, S, Ca, Fe) have been pre–computed using the publicly available CLOUDY photo–ionisation code (Ferland et al. 1998) for an optically thin gas in (photo–)ionisation equilibrium. This procedure to compute cooling rates avoids the assumptions of collisional ionisation equilibrium and solar relative abundances, which were underlying in the prescription based on cooling rates from Sutherland and Dopita (1993), that we adopted in previous simulations (e.g. Tornatore et al. 2007; Fabjan et al. 2010).

A first set of radiative simulations includes star formation and the effect of feedback triggered by supernova (SN) explosions (`CSF` hereafter). As for the star formation model, gas particles above a given threshold density are treated as multiphase, so as to provide a sub–resolution description of the interstellar medium, according to the model originally described by Springel and Hernquist (2003a). Within each multiphase gas particle, a cold and a hot-phase coexist in pressure equilibrium, with the cold phase providing the reservoir of star formation. The production of heavy elements is described by accounting for the contributions from SN-II, SN-Ia and low and intermediate mass stars, as described by Tornatore et al. (2007). Stars of different mass, distributed according to a Chabrier IMF (Chabrier 2003), release metals over the time-scale determined by the mass-dependent life-times of Padovani and Matteucci (1993). Kinetic feedback contributed by SN-II is implemented according to the model by Springel and Hernquist (2003a): a multi-phase star particle is assigned a probability to be uploaded in galactic outflows, which is proportional to its star formation rate. In the `CSF` simulation set we assume ${\rm v_w} = 500\,{\rm km\,s^{-1}}$ for the wind velocity, while assuming a mass–upload rate that is two times the value of the star formation rate of a given particle.

Another set of radiative simulations is carried out by including the same physical processes as in the `CSF` case, with a lower wind velocity of ${\rm v_w} = 350\,{\rm km\,s^{-1}}$, but also including the effect of AGN feedback (`AGN` set, hereafter). The model for AGN feedback is based on the original implementation presented by Springel et al. (2005) (SMH), with feedback energy released as a result of gas accretion onto supermassive black holes (BH). In this AGN model, BHs are described as sink particles, which grow their mass by gas accretion and merging with other BHs. Gas accretion proceeds at a Bondi rate, and is limited by the Eddington rate. Once the accretion rate is computed for each BH particle, a stochastic criterion is used to select the surrounding gas particles to be accreted. Unlike in SMH, in which a selected gas particle contributes to accretion with all its mass, we included the possibility for a gas particle to accrete only with a slice of its mass, which corresponds to 1/4 of its original mass. In this way, each gas particle can contribute with up to four "generations" of BH accretion events, thus providing a more continuous description of the accretion process.

Eddington-limited Bondi accretion produces a radiated energy which corresponds to a fraction $\epsilon_r = 0.1$ of the rest-mass energy of the accreted gas, which is determined by the radiation efficiency parameter ϵ_r. The BH mass is correspondingly decreased by this amount. A fraction of this radiated energy is thermally coupled to the surrounding gas. We use $\epsilon_f = 0.1$ for this feedback efficiency, which increases by a factor of 4 when accretion enters in the quiescent "radio" mode and drops below one-hundredth of the limiting Eddington rate (e.g. Sijacki et al. 2007; Fabjan et al. 2010).

Additionally, we introduced some technical modifications of the original implementation, which will be briefly described here. One difference with respect to the original SMH implementation concerns the seeding of BH particles. In the SMH model, BH particles are seeded in a halo whenever it first reaches a minimum (total) friends-of-friends (FoF) halo mass, such as to guarantee that a halo is resolved with at least 50 DM particles. In order to guarantee that BHs are seeded only in halos where star formation took place, in our implementation we look for FoF groups in the distribution of star particles, by grouping them with a linking length of about 0.05 times the mean separation of the DM particles. This linking length is thus smaller than that, 0.15–0.20, originally used, to identify virialised halos. In the simulations presented here, a minimum mass of $4 \times 10^{10}\, h^{-1} M_\odot$ is assumed for a FoF group of star particles to be seeded with a BH particle. Furthermore, we locate seeded BHs at the potential minimum of the FoF group, instead of at the density maximum, as originally implemented by SMH. We also enforce a more strict momentum conservation during gas accretion and BH mergings. In this way a BH particle remains within the host galaxy, when it becomes a satellite of a larger halo. In the original SMH implementation, BHs were forced to remain within the host galaxy by pinning them to the position of the particle found having the minimum value of the potential among all the particles lying within the SPH smoothing length compute at the BH position. We verified that an aside effect of this criterion is that, due to the relatively large values of SPH smoothing lengths, a BH can be removed from the host galaxy whenever it becomes a satellite, and is spuriously merged into the BH hosted in the central halo galaxy (see Dolag et al. 2013 in preparation for a detailed description). This description of BHs provides a realistic description of the observed relation between stellar mass and BH mass, and of the observed BH-mass function and luminosity function (see Hirschmann et al. 2013, in preparation).

2.3 Identification of clusters

The identification of clusters proceeds by running first a FoF algorithm in the high–resolution regions, which links DM particles using a linking length of 0.16 times the mean interparticle separation. The center of each halo is then identified with the position of the DM particle, belonging to each FoF group, having the minimum value of the gravitational potential.

Starting from this position, and for each considered redshift, a spherical overdensity algorithm is employed to find the radius R_Δ encompassing a mean density of Δ times the critical cosmic density at that redshift, $\rho_c(z)$. In the present work, we consider values of the overdensity[3] $\Delta = 2500$, 500 and 200. For the sake of completeness, we also consider the virial radius which defines a sphere enclosing the virial density $\Delta_{\rm vir}(z)\rho_c(z)$, predicted by the spherical collapse model ($\Delta_{\rm vir} \approx 93$ at $z = 0$ and ≈ 151 at $z = 1$ for our cosmological model). In total, we end up with about 70 clusters and groups having $M_{vir} > 1 \times 10^{14} h^{-1} M_\odot$ at $z = 0$.

Throughout this work all the quantities of interest will be evaluated at the four different characteristic radii. Therefore, for each cluster, the hot gas, stellar, and baryonic mass fractions within a given radius R_Δ are defined, respectively, as

$$f_{\rm g}(< R_\Delta) = \frac{M_{\rm g}(< R_\Delta)}{M_{\rm tot}(< R_\Delta)} \tag{1}$$

$$f_*(< R_\Delta) = \frac{M_*(< R_\Delta)}{M_{\rm tot}(< R_\Delta)} \tag{2}$$

$$f_{\rm b}(< R_\Delta) = \frac{M_{\rm g}(< R_\Delta) + M_*(< R_\Delta)}{M_{\rm tot}(< R_\Delta)}\,. \tag{3}$$

3 BARYON CONTENT OF CLUSTERS

Figures 1, 2, and 4 show, respectively, the baryon, stellar, and gas mass fractions of our simulated clusters as a function of cluster mass M_{500}. Only clusters with $M_{500} \gtrsim 3 \times 10^{13}\, h^{-1} M_\odot$ within our `NR`, `CSF`, and `AGN` runs are shown. In order to compare with observational data, we use some representative observational samples, mainly those from Lin et al. (2003), Gonzalez et al. (2007), Giodini et al. (2009), Laganá et al. (2011), and Zhang et al. (2011). For all the observational data sets we compare with, we compile in Table 1 the best fittings obtained for the baryon, gas, and stellar mass fractions.

Before comparing our results with observational data, let us briefly describe the main properties of the different observational samples (for further details, we refer to their corresponding papers). Knowing how the observational data have been derived is important to understand not only discrepancies between our simulations and the observations but also the differences between the observational results.

Laganá et al. (2011) and Zhang et al. (2011) investigate the baryon mass content for a subsample of 19 clusters of galaxies extracted from the X-ray flux-limited sample HIFLUGCS. For these clusters, the above authors measure total masses and characteristic radii on the basis of a rich optical spectroscopic data set, the physical properties of the intra-cluster medium using *XMM-Newton* and *ROSAT* X-ray data, and total (galaxy) stellar masses utilizing the DR-7 SDSS multi-band imaging. Using gas mass measurements from X–ray observations, Laganá et al. (2011) use a scaling relation between the gas and the total mass to determine the total cluster mass. Following a different approach, Zhang et al. (2011) derive cluster masses from measurements of the "harmonic" velocity dispersion as described by Biviano et al. (2006). In both studies, to

[3] The corresponding radii aproximately relate to the virial radius as $(R_{2500}, R_{500}, R_{200}) \approx (0.2, 0.5, 0.7)\, R_{\rm vir}$ (e.g., Ettori et al. 2006).

obtain the contribution of galaxies to the stellar mass, they use the optical data for selected member galaxies within R_{500} to compute their luminosity function in the i-band, performing an analytical fit using two Schechter functions. Then, they adopt different mass-to-light ratios for ellipticals and spirals, taken from Kauffmann et al. (2003) assuming a Salpeter (1955) IMF, to compute the stellar mass from the optical luminosity. In Lin et al. (2003) they use the observed X-ray mass-temperature relation together with published X-ray emission weighted mean temperatures, *2MASS* second incremental release NIR data, and X-ray imaging data to explore trends in the NIR and X-ray properties of a sample of 27 nearby galaxy clusters. The total mass of the clusters in this sample is estimated from an observed $M_{500} - T_X$ relation. The stellar masses are obtained from the cluster luminosity function as derived from the magnitudes in the K_s band. Using a Schechter function they estimate the total cluster luminosity and, finally, they obtain the total stellar masses, as contributed by satellite galaxies and BCG, by multiplying the total luminosity by the average stellar mass-to-light ratio for each cluster which takes into account the varying spiral galaxy fraction as a function of the cluster temperature. In Giodini et al. (2009), 91 candidate X-ray groups/poor clusters at redshift $0.1 \leqslant z \leqslant 1$ are selected from the COSMOS 2 deg^2 survey, based only on their X–ray luminosity and extent. They use X-ray detection, gravitational lensing signal, optical photometric and spectroscopic data of the clusters and groups identified in the COSMOS survey. Total cluster masses are derived from a $L_X - M_{500}$ relation. The stellar mass of a galaxy is obtained from the conversion of the K_s-band luminosity using an evolving galaxy-type dependent stellar mass-to-K_s-band luminosity ratio. Since this sample is mostly composed of groups, it is complemented with the 27 nearby X-ray selected clusters in the sample by Lin et al. (2003), where the total and stellar masses are derived in a consistent manner. To reduce systematic effects, they use the scaling relations in Pratt et al. (2009), based on hydrostatic mass estimates, to derive the total gas fractions in both samples. The total sample of 118 groups and clusters with $z \leqslant 1$ spans a range in M_{500} of $\sim 10^{13}$–10^{15} $M_{\odot}$. On the other hand, Gonzalez et al. (2007) use an optical sample of 24 nearby clusters and groups for which they obtain drift scan imaging in Gunn i using the Great Circle Camera on Las Campanas 1 m Swope telescope. This sample is composed of systems at $0.03 \leqslant z \leqslant 0.13$ that contain a dominant BCG. To obtain the total masses and cluster radii they derive calibrations of the $\sigma - R_{500}$ and $\sigma - M_{500}$ relations using the clusters from Vikhlinin et al. (2006) that also have published velocity dispersions. They determine the luminosity of the BCG+ICL component by fitting the surface brightness distribution in each cluster out to a radius of 300 kpc from the BCG. Then, they use the separate $r^{1/4}$ best-fit profiles of these two components to build a two-dimensional model image from which they determine the flux within a given circular aperture. On the other hand, the luminosity of the cluster galaxies lying within the same aperture is computed by summing the flux of all galaxies fainter than the BCG and brighter that $m_I = 18$. Then, they use a relation for the luminosity dependence of the mass-to-light ratio in the I band to convert from total luminosity to total stellar mass. Since they lack measurements of the mass of hot gas in the ICM for this sample, they fit the behaviour of the stellar mass fraction with cluster mass and use this relation to derive total baryon fractions for clusters with published X-ray gas fractions. We also compare our results for the gas mass fractions with a sample of observed groups and clusters at $z \leqslant 0.2$ selected from the X-ray samples of Vikhlinin et al. (2006), Arnaud et al. (2007) and Sun et al. (2009). These authors computed gas mass fractions at R_{500} from hydrostatic mass estimates for a combined sample containing 41 systems within a range of masses of [1.5×10^{13},1.1×10^{15}] $M_{\odot}$.

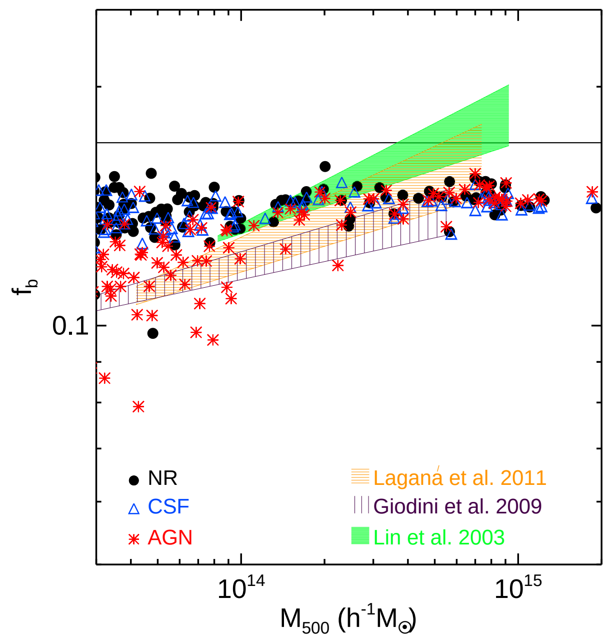

Figure 1. Baryon mass fraction as a function of cluster mass M_{500}. Results from our `NR`, `CSF`, and `AGN` runs are represented by black circles, blue triangles, and red stars, respectively. The observational samples from Lin et al. (2003), and Laganá et al. (2011) are shown as shaded regions in green and orange, respectively, whereas the sample from Giodini et al. (2009) is represented by a grey-striped area. These regions correspond to the best fits obtained together with their corresponding errors (see Table 1). The horizontal continuos line stands for the cosmic baryon fraction assumed in our simulations.

Due to the different observational methods used to derive the main cluster properties, some differences are expected between the baryon census provided by these samples. In addition, it is necessary to point out that, when comparing the stellar mass fractions, only Gonzalez et al. (2007) take into account the contribution of the ICL component. In our case we also consider the total (galaxies+ICL) stellar contribution within clusters. In the following, after comparing simulation results to the observed total baryon budget in clusters and groups, we will dissect the separate contribution of stars and of hot X–ray emitting gas.

3.1 Baryon mass fraction

As shown in Fig. 1, in our `NR` simulations the baryon mass fractions within R_{500} is nearly independent of cluster mass and is systematically lower than the assumed cosmic value by $\lesssim 10$ per cent. This result is consistent with previous analyses, also based on SPH simulations (e.g. Eke et al. 1998; Ettori et al. 2006), which also found a comparable underestimate in the cluster baryon fraction. Using a Eulerian AMR code, Kravtsov et al. (2005) also measured a cluster baryon fraction in non–radiative simulations below the cosmic value, although in their case the underestimate was of about 5 per cent within R_{500}. A similar behaviour is also found for our radiative `CSF` simulations, thus indicating that the processes of star formation and galactic winds triggered by SN explosions determine

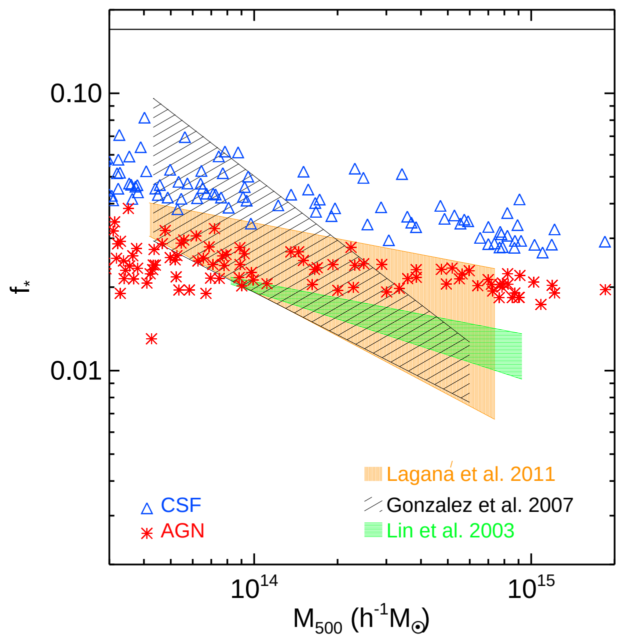

Figure 2. Stellar mass fraction as a function of cluster mass M_{500}. Results from our radiative simulations, `CSF` and `AGN`, are represented by blue triangles and red stars, respectively. The observational samples from Lin et al. (2003) and Laganá et al. (2011) are shown as shaded regions in green and orange, respectively, whereas the sample from Gonzalez et al. (2007) is represented by a black-striped area. These regions represent the best fits obtained from each observational sample as compiled in Table 1. The horizontal continuos line stands for the assumed baryon mass fraction in our simulations.

the fraction of baryons to be converted into stars, without however changing the overall baryon budget within R_{500}.

As we include the effect of BH feedback in the `AGN` simulations, there is a significant baryon depletion in poor clusters and groups, whereas results are nearly the same as for the `NR` and `CSF` cases for $M_{500} \gtrsim 2 \times 10^{14}\, h^{-1} M_{\odot}$. This result of a decreasing baryon fraction at low masses is in line with those presented by Fabjan et al. (2010), Puchwein et al. (2010), and McCarthy et al. (2011), who also included the effect of BH feedback in their simulations of galaxy groups and clusters. This effect of baryon depletion within groups witnesses the efficiency that BH feedback has in displacing gas outside forming halos. This effect takes mostly place at relatively high redshift, $z \simeq 2-3$, around the peak of the BH accretion efficiency. At these epochs, the energy extracted from BHs increases the gas entropy to levels such to prevent this gas from being subsequently re-accreted within group–sized halos (e.g. McCarthy et al. 2011).

As for the comparison of simulation results with observations, it is quite remarkable that a good agreement is only achieved for the `AGN` model. This result confirms that a feedback mechanisms only based on SN explosions can not be responsible for the decreasing trend of the baryon budget within halos of decreasing mass (e.g. Short and Thomas 2009).

3.2 Stellar mass fraction

We show in Fig. 2 the stellar mass fraction in our radiative runs. As expected, the effect of including AGN feedback is that of reducing the stellar content of galaxy systems by about 30 per cent, nearly independent of cluster mass. As for the comparison with previous simulation results, we note that the clusters simulated by Puchwein et al. (2010) with AGN feedback have stellar fractions, which are larger by about a factor of 2 than the stellar fractions found in our `AGN` simulation. We can understand this difference by keeping in mind that the amount of stars formed in simulations depends rather sensitively on how the SN feedback is included (e.g., Springel and Hernquist 2003b; Borgani et al. 2006). In the simulations by Puchwein et al. (2010), all the feedback from star formation was injected thermally, without including kinetic SN feedback as we did in our simulations. As these authors also noticed (see their Sect. 3.1), using kinetic feedback, in addition to thermal feedback, can significantly reduce the amount of stars formed in their simulations by a factor of 2, resulting, therefore, in a good consistency with the stellar mass fractions obtained in our `AGN` runs. Common to this kind of simulations is that the BH accretion rate, and hence of the amount of feedback energy, is directly derived from simulated hydrodynamical quantities by means of a sub–resolution accretion model. Following an alternative approach, Young et al. (2011) adopted the hybrid description of Short and Thomas (2009), which couples a semi-analytic model of galaxy formation to a cosmological N-body/SPH simulation, to analyse the baryon fractions in clusters of galaxies. In this approach, the energy released to the ICM by SNe and AGN is computed from a semi-analytic model and injected into the baryonic component of a non-radiative hydrodynamical simulation. Given that semi-analytic models are tuned to reproduce the properties of observed galaxies, the main advantage of this approach is that the energetic feedback is originated from a realistic population of galaxies. As a potential limitation of this approach, radiative cooling is not included in the simulations. As a result, Young et al. (2011) obtain stellar fractions in massive clusters that agree better with observations than in self-consistent hydrodynamical simulations, but they considerably underestimate star formation in groups.

As for the comparison with observational results, we find that our `CSF` simulations produce a too large stellar fraction in massive galaxy clusters, independent of the observational data set we compare to. While simulations with AGN feedback give results closer to observations, the level of agreement is quite sensitive to the observational result we refer to. For instance, a comparison with the results by Gonzalez et al. (2007) would imply that in no case simulations reproduce the steep mass dependence of f_*, independently of the feedback mechanism included (see also Andreon 2010). On the other hand, a closer agreement with observations would be obtained from Fig. 2 by referring instead to the results by Laganá et al. (2011). The inclusion of the ICL component in the analysis by Gonzalez et al. (2007) could explain part of the difference with respect to Laganá et al. (2011), although apparently not all of it (see also Zhang et al. 2011). Clearly, some caution must be used when comparing observational and simulated samples, owing also to the different approaches followed by different authors to measure stellar mass fraction from data, the dependence of the inferred stellar mass on the choice of the IMF (e.g., Laganá et al. 2011; Leauthaud et al. 2012), and systematic uncertainties in the measurement of the total cluster mass.

In order to better understand how much intra–cluster stars contribute to the total stellar mass budget in our simulations, it is im-

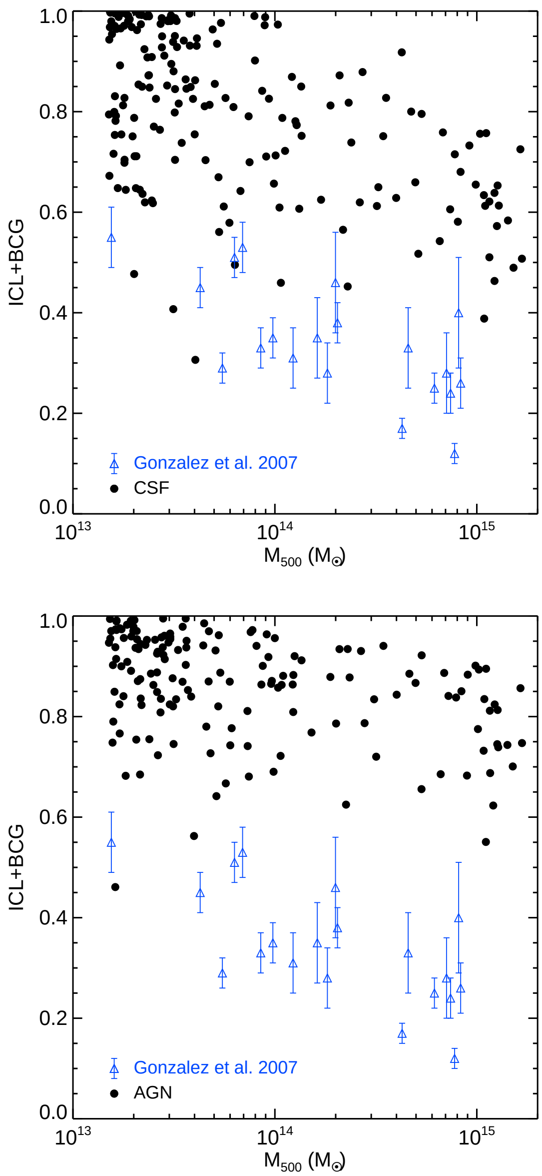

Figure 3. Fraction of the stellar mass found in the BCG+ICL component as a function of cluster mass M_{500}. The upper panel shows the values obtained from our radiative runs without AGN feedback, the `CSF` runs, while the lower panel displays the results obtained from our runs including AGN. We compare our results with the observed BCG+ICL luminosity fractions from Gonzalez et al. (2007).

portant to distinguish between the stellar content of the BCGs, of the satellite galaxies and of the ICL component. Aside from some exceptions, the central galaxy in a cluster, which is the closest to the minimum of the cluster potential well, is typically also the brightest cluster galaxy. Therefore, for simplicity, we will use the abbreviation BCG when referring to the central galaxy of a simulated cluster or group. Due to its low surface brightness, observations of the ICL component, which is a smoothly distributed stellar component typically peaked around the BCG but extended to larger radii, are difficult, resulting in a significant uncertainty in the current observational constraints of the amount of ICL present in clusters (e.g., Zibetti et al. 2005; Gonzalez et al. 2007).

While identifying member galaxies within galaxy clusters in hydrodynamical simulations is a relatively straightforward task (e.g., Onions et al. 2012), distinguishing between stars in the diffuse stellar component and in the central galaxy is not so trivial. In order to do so, we use a modified version of the SUBFIND algorithm (Springel et al. 2001; Dolag et al. 2009). In its original version (Springel et al. 2001), SUBFIND identifies star particles that are associated with satellite galaxies residing within a cluster–sized halo. All the star particles not associated to satellite galaxies are assigned to the central galaxy of the main halo, without distinguishing between those associated to the actual BCG and those belonging to the surrounding ICL. Dolag et al. (2009) pointed out that BCG and ICL stars show different phase–space distributions and implemented this property in SUBFIND, making it able to distinguish among the different stellar components. For more details about this modified version of SUBFIND we refer the reader to the work by Dolag et al. (2010).

An intrinsic difficulty in properly comparing observations and simulation results on the amount of ICL is due to the intrinsically different procedures usually adopted to identify diffuse stars in real and in simulated data. While observations generally use a criterion based on surface brightness limit, ICL analysis in simulations is generally based on identifying star particles that are not gravitationally bound to galaxies. In addition, very faint ICL component can not be detected in observations while it is present in simulations. While we defer to a future paper a homogeneous comparison between intra-cluster light in observations and simulations, we show here a comparison between the results by Gonzalez et al. (2007) on the amount of stars present in BCG and ICL, and corresponding simulation results. In fact, considering the total stellar content of BCG and ICL overcomes at least the ambiguity in the surface brightness limit below which the BCG halo has to be considered as part of the BCG. This also avoids choosing among the different ICL definitions in the literature (e.g. Zibetti et al. 2005) allowing, therefore, a more straightforward comparison between our results and other simulations and observational studies. In Fig. 3 we plot the fractions of stellar mass found in the BCG+ICL components in our simulated sample of clusters with $M_{500} \geqslant 1.5 \times 10^{13} M_{\odot}$. Results obtained from our radiative simulations without and with AGN feedback (`CSF` and `AGN` runs), are shown in the top and bottom panels, respectively. We compare our data with the observational constraints on the BCG+ICL fraction from Gonzalez et al. (2007), shown as blue triangles with error bars.

Although our results in general confirm a decreasing trend with cluster mass of the fraction of stars contributed by BCG and ICL, they predict a too large value of this fraction in comparison with the observational result by Gonzalez et al. (2007). In the `CSF` simulations we obtain BCG+ICL fractions of roughly ~ 60 per cent for massive clusters, and of about ~ 90 per cent for groups. These values are larger than those observed by Gonzalez et al. (2007), especially for massive clusters. However, we have to take into account that there is some uncertainty in the mass assigned to the BCG and ICL components due to the analysis method used for separating them (see, for instance, Puchwein et al. 2010).

In addition, given that the distribution of the BCG+ICL component is more concentrated than the distribution of the satellite galaxies, these values are sensitive to the radius inside which they are measured.

When AGN feedback is included, we find an even larger fraction of stars in the BCG+ICL component, a result that is consistent with that presented by Puchwein et al. (2010). The reason for this result is that, although the stellar mass of the BCG+ICL component decreases when including AGN feedback, the total stellar mass de-

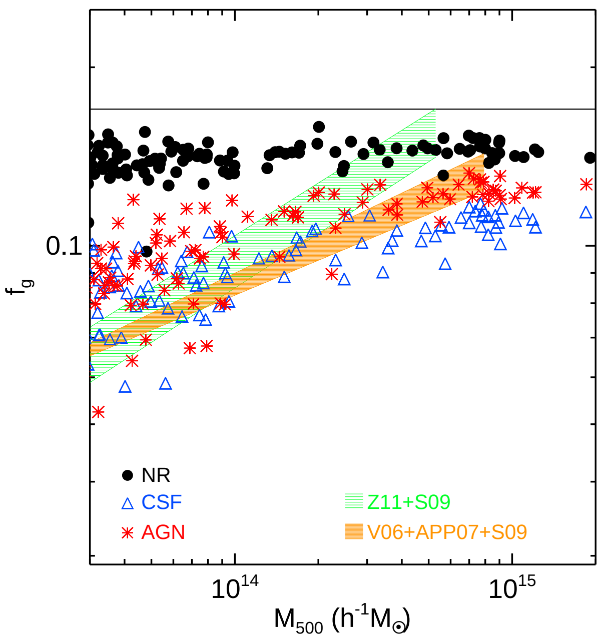

Figure 4. Gas mass fraction as a function of cluster mass M_{500}. Results from our `NR`, `CSF`, and `AGN` runs are represented by black circles, blue triangles and red stars, respectively. We compare our results with two different observational samples: a combined sample of 41 clusters and groups from Vikhlinin et al. (2006), Arnaud et al. (2007) and Sun et al. (2009) (V06+APP07+S09), shown as the orange region, and the sample obtained from the combination of the data by Zhang et al. (2011) and Sun et al. (2009) (Z11+S09), shown as the green area (see Table 1). The horizontal continuos line marks the cosmic value of the baryon mass fraction assumed in our simulations.

creases even more (see Fig. 2). A relative increase of stars in BGC and ICL is the consequence of the combination of two different effects. On the one hand, the effect of AGN feedback is mainly that of truncating the star formation of clusters at high redshift, $z\lesssim 3$ (e.g. Fabjan et al. 2010; McCarthy et al. 2011). On the other hand, most of the dynamical origin of the ICL is associated with the assembly of the BGC (e.g. Murante et al. 2007). Since mergers continue to take place after star formation is quenched by AGN feedback, they keep unbounding stars from galaxies into the diffuse intra–cluster components. Since this process is not compensated by fresh star formation in the presence of AGN feedback, the net effect is that of increasing the fraction of stars that end up in the ICL. In a future analysis (Cui et al., in preparation) we will carry out a more detailed comparison of ICL inventory and properties in simulations, by reproducing in their analysis the same criteria to identify ICL as in observational data.

3.3 Gas mass fraction

As shown in Fig. 4, including radiative physics in the simulations has the expected effect of decreasing the gas fraction within R_{500} (see also Kravtsov et al. 2005; Fabjan et al. 2010; Puchwein et al. 2010; McCarthy et al. 2011; Young et al. 2011; Sembolini et al. 2012), by an amount which is more pronounced in poor clusters and groups. As for the effect of including different feedback mechanisms, a comparison between our simulations with and without AGN feedback shows that the two feedback schemes predict rather similar values of the gas fraction at the mass scale of groups while simulations including AGN feedback predicts slightly more gas within large clusters. Clearly, the similar values of f_g in groups do not imply that feedback does not have any effect on such systems. In fact, a comparison with Figs. 1 and 2 highlights that AGN feedback tends to remove baryons from the potential wells of galaxy groups. At the same time, suppression of star formation partially prevents removal of gas from the hot diffuse phase within R_{500}, thereby acting as a compensating effect such that the resulting gas fraction turns out to be similar for the two feedback schemes. As for higher–mass halos, AGN feedback becomes less efficient in removing baryons from halos (see also Fig. 1), so that suppression of star formation causes a slightly larger fraction of baryons to remain in the diffuse phase, so that f_g in this case increases as a result of a more efficient feedback. This differential effect of AGN feedback in low– and high–mass halos is generally quite weak, although it goes in the direction of better reproducing the observed trend of f_g with halo mass.

From the analysis of Fig. 4 we conclude that, in general, our results on the values of f_g, especially at the scale of rich clusters, are in better agreement with the observational results obtained by Vikhlinin et al. (2006), Arnaud et al. (2007), Sun et al. (2009), and Zhang et al. (2011) when AGN feedback is included.

4 CALIBRATION OF THE BARYONIC BIAS

After having compared simulation results on the different baryonic components with observational data, in this Section we use our results to calibrate the different baryonic depletions and to analyse their dependences on redshift, baryonic physics and cluster radius.

For the sake of comparison with previous works, we define the gas, stellar and baryon depletion factors (from now on $Y_{\rm g}$, Y_*, and $Y_{\rm b}$, respectively) as the ratios between $f_{\rm g}$, f_* and $f_{\rm b} = f_{\rm g} + f_*$, and the cosmic value adopted in the present simulations, $\Omega_{\rm b}/\Omega_{\rm m} = 0.167$. Accordingly, we should measure $Y_{\rm b} = 1$ within clusters as long as they are fair containers of cosmic baryons. Any deviation from this value has to be interpreted as due to the presence of a “baryonic bias”, whose origin can be due either to gas dynamical effects at play during the hierarchical assembly of clusters, or to star formation and feedback effects that causes sinking or expulsion, respectively, of baryons from the cluster potential wells. The non-radiative simulations of hot, massive clusters published by Eke et al. (1998) (see also Crain et al. 2007) give $Y_{b,0} = 0.83 \pm 0.04$ at R_{2500}, and are consistent with no redshift evolution of Y_b for $z < 1$. Nevertheless, simulations including different models of baryonic physics (Kay et al. 2004; Ettori et al. 2006; Crain et al. 2007; Nagai et al. 2007; Short et al. 2010) allow for a range of evolutions. We note, however, that these previous analyses either lack sufficient statistics of massive systems, which are relevant for cosmological applications, or the inclusion of an efficient feedback mechanism, like that provided by AGN, which provides a realistic description of star formation in the central regions of galaxy clusters.

The results that we will present in the following are relevant to test the robustness of the calibration through simulations of the baryon bias, i.e. of the deviation of the baryon content of clusters from the cosmic value, that one needs to correct for in the cosmological application of the gas mass fraction.

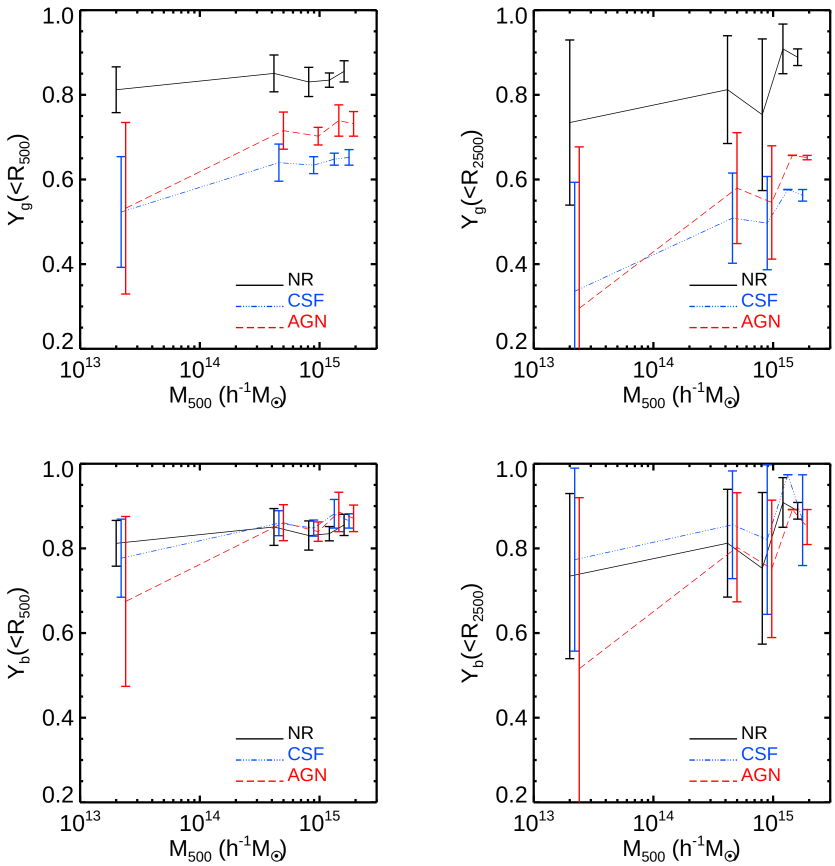

Figure 5. Mass dependence of the gas depletion factor $Y_{\rm g}$ (upper row), and total baryon depletion factor $Y_{\rm b}$ (lower row), computed at R_{500} and R_{2500} (left and right columns, respectively). Results are shown for the set of simulated clusters with $M_{500} \gtrsim 1 \times 10^{13}\, h^{-1} M_\odot$ identified at $z = 0$ within our `NR`, `CSF`, and `AGN` runs. Clusters are binned in five linearly spaced mass bins. Different line types represent the mean values obtained within each mass bin for each of our simulations, while error bars stand for 1σ standard deviations computed within the subset of clusters within each mass bin. For reasons of clarity, lines corresponding to the different physical models have been slightly displaced along the x-axis.

4.1 Radial dependence of the baryonic bias

We show in Fig. 5 the mass dependence of $Y_{\rm g}$ and $Y_{\rm b}$ at $z = 0$ (up and bottom row, respectively) within the two characteristic radii R_{500} (left column) and R_{2500} (right column). As for R_{500}, it typically corresponds to the most external radius out to which detailed X–ray observations, possibly in combination with Sunyaev–Zeldovich (SZ) observations (e.g. Planck Collaboration et al. 2011), allow one to trace the gas content within clusters, while R_{2500} is the typical radius within which gas content is traced for distant clusters, when using the evolution of the gas fraction in clusters as a cosmological probe (e.g. Allen et al. 2008). Therefore, for these two radii, we show the mean values of the gas and baryon depletion factors obtained for our sample of simulated clusters binned in five linearly equi-spaced bins in M_{500}. All clusters with $M_{500} \gtrsim 1 \times 10^{13}\, h^{-1} M_\odot$ have been considered. The mean values within each mass bin are shown along with error bars representing one standard deviation within the corresponding mass interval.

The left panel of this figure summarizes the simulations results shown in Figs. 1 and 4. Using the mass binning, it is now more clear that the depletion in baryon content within R_{500} is more pronounced and with a stronger mass dependence for the simulations including AGN feedback, at least for low–mass systems. As already discussed, the larger baryon depletion in clusters simulated with AGN feedback is the result of the efficiency of this feedback mechanism in removing baryons from the potential wells of forming groups at redshift $z \sim 2$–3, around the peak of gas accretion onto SMBHs. On the other hand, for masses $M_{500} \gtrsim 2 \times 10^{14}\, h^{-1} M_\odot$ we find that the baryon fraction within R_{500} underestimates the cosmic value by about 15 per cent, nearly independent of mass and of the physics included in the simulations. The r.m.s. dispersion around this values is of about 3 per cent for the `NR` and `CSF` simulations, which increases to about 5 per cent for the `AGN` simulations. This result for Y_b is different from the behaviour of gas depletion, which shows no flattening for high–mass systems. Furthermore, values of Y_g for the AGN simulations are systematically larger than for the radiative simulations including only SN feedback, as a result of the suppressed star formation in the former case.

These results suggest that a mass–independent correction can be calibrated from simulations to infer the cosmic baryon fraction from the corresponding quantity derived for massive clusters, a correction that is likely independent of the uncertain knowledge of the physical processes at play in the ICM. However, these results also highlight that accurately recovering the baryon fraction from gas mass measurements involves accurately accounting for a correction associated to stellar mass, which generally depends on cluster total mass.

Results on gas and baryon depletions are somewhat different within R_{2500} (right column of Fig. 5). In this case, both Y_g and Y_b show as steady increase with cluster mass, with no evidence for a flattening at high masses, and a larger intrinsic scatter in their values. Furthermore, a small but sizeable dependence of Y_b on the physics included in the simulations exists even for the highest mass systems. Quite interestingly, the largest values of Y_b are obtained for the CSF simulations, as a result of the strong overcooling, not efficiently counteracted by the SN feedback, which causes a large amount of baryons to condense in the central halo regions. On the other hand, the smallest Y_b value is obtained in the presence of AGN feedback, which is quite efficient in displacing gas from central regions even for the most massive clusters. In general, these results indicate that the baryon depletion within R_{2500} is more sensitive to the detailed description of the feedback process which regulates the cooling–heating cycle. As a result, care must be taken in the use of simulations to exactly calibrate the correction for baryon depletion to observations providing gas and baryon fractions at such smaller cluster–centric radii.

As shown in Fig. 5, the population of the most massive clusters is characterized, especially within R_{500}, both by a remarkably small intrinsic scatter in their baryon budget, and by a stability against the different physical descriptions of the ICM. As such these massive clusters are those which can be more reliably calibrated for cosmological applications of the cosmic baryon fraction test. Therefore, in the following we will restrict the analysis of these radial distributions only to clusters with $M_{500} > 2\times10^{14}\,h^{-1}M_\odot$. Within our simulations we identify about 40 of such objects at $z = 0$, a number that reduces to 10 at $z = 1$.

The effect of the different physical models considered in our simulations on the distribution of baryons can be better understood from the analysis of the radial distribution of the different baryonic components within clusters. Figure 6 shows the mean radial distribution out to $4 \times R_{500}$ of the baryonic, gas and stellar depletions at $z = 0$ (left column) and $z = 1$ (right column) for our subsample of massive clusters within each of the physical schemes adopted in our simulations.

Regardless of the baryonic processes included in our re-simulations, the baryonic depletion at $z = 0$ for radii $r/R_{500} \geqslant 0.4$ approaches a value of ~ 85 per cent of the cosmic value, showing similar values at $z = 1$ but with larger scatter. This baryonic depletion starts to converge to the expected value at $r \sim 3 \times R_{500}$, consistent with results found in previous simulations (e.g., Eke et al. 1998; Ettori et al. 2006). In these outer regions of clusters, the gas mass dominates the baryon budget. In general, the gas depletion increases from inner to outer regions and shows slightly higher values at low redshifts. On the contrary, the stellar depletion decreases when moving towards more external regions and, therefore, if we move towards more internal radii ($r/R_{500} \leqslant 0.1$) the stellar mass clearly dominates the baryon content in the radiative runs. In these central regions, the non-radiative simulations produce lower values of the baryonic depletion than the radiative runs which are, indeed, characterised by a steep inner slope. When cooling and star formation are included, the gas can cool and form stars and, therefore, it sinks deep into the potential wells of the clusters. If AGN feedback is also added, its main effect is that of heating the surrounding gas producing, therefore, smaller baryon mass fractions in the cluster center. In general, the different baryonic depletions obtained in the inner regions of clusters from the CSF and AGN simulations are comparable with each other. However, we note that while the baryon and stellar depletions at $z = 1$ are higher in the CSF simulations, this is inverted at $z = 0$. The reason for this lies in the stronger feedback associated to galactic winds in the CSF model. In fact, the effect of AGN feedback at $z = 1$ is still sub-dominant. As a result, at this redshift the higher wind efficiency of CSF with respect to AGN model turns into a reduced effect of cooling, which manifests itself both in the total amount of baryons sinking in the cluster potential wells and in the amount of stars produced. It is only at $z < 1$ that AGN feedback prevails, thereby reverting these trends.

In Fig. 7 we show the comparison between the cumulative gas mass fraction profile, $f_g(< r)$, in our simulations and from the observational results by Pratt et al. (2010). The cumulative gas profiles within each of our physical models have been computed at $z = 0$ out to $4\times R_{500}$ for our subsample of massive clusters, which lay in the temperature range $2 - 10$ keV. Pratt et al. (2010) examine the radial entropy and gas distributions of 31 nearby galaxy clusters from the Representative *XMM-Newton* Cluster Structure Survey (REXCESS, Böhringer et al. 2007). This sample, which includes clusters with temperature in the range 2–9 keV, has been selected in X-ray luminosity only, with no bias towards any particular morphological type. According to their central densities, clusters in this sample have been classified in cool core systems (CC) and in morphologically disturbed or non-cool core (NCC) systems[4].

As we can infer from Fig. 7, our radiative simulations are quite successful in reproducing the observed gas profiles for the NCC population out to the limit of the observations. However, as already reported by other authors (see, for instance, Young et al. 2011), radiative simulations fail in matching the profiles associated with the CC clusters, which show flatter gas mass fraction profiles in their inner regions.

4.2 Redshift evolution of the baryonic bias

Besides assessing the stability of the baryon and gas depletions at $z = 0$, measuring the evolution of such quantities is also required for measurements of the gas fraction over a large redshift baseline to be used to recover the redshift–distance relation. A comparison of the profiles of baryon and gas depletion computed at $z = 0$ and $z = 1$ (see Fig. 6) shows that outside the central regions this evolution is generally rather mild.

To quantify this evolution, we compute the values of the depletion factors at different redshifts, $z = 0$, 0.3, 0.7, 0.8 and 1. At each redshift, the analysis is done only on those clusters having mass $M_{500} > 2 \times 10^{14}\,h^{-1}M_\odot$. We show the redshift evolution of these quantities at R_{500} and R_{2500} in the left and right panels of Fig. 8, respectively, along with their respective intrinsic scatters, given by the error bars. A compilation of these values, for the different redshifts and simulation sets, are also reported in Table 2.

In order to parameterize a possible evolution of the values of the depletion factors, we use the expression

$$Y_i(z) = Y_{0,i}(1 + \alpha_{Y_i} z)\,, \qquad (4)$$

where the subscript i is equal to b or g when referring to the total baryon or gas content, respectively. The values of the parameters $Y_{0,i}$ and α_{Y_i} are computed through a χ^2 minimization procedure,

[4] More especifically, this sample of 31 clusters contains 10 CC and 12 NCC systems. The rest of systems, which have not been morphologically classified, are shown in Fig. 7 as NCC clusters.

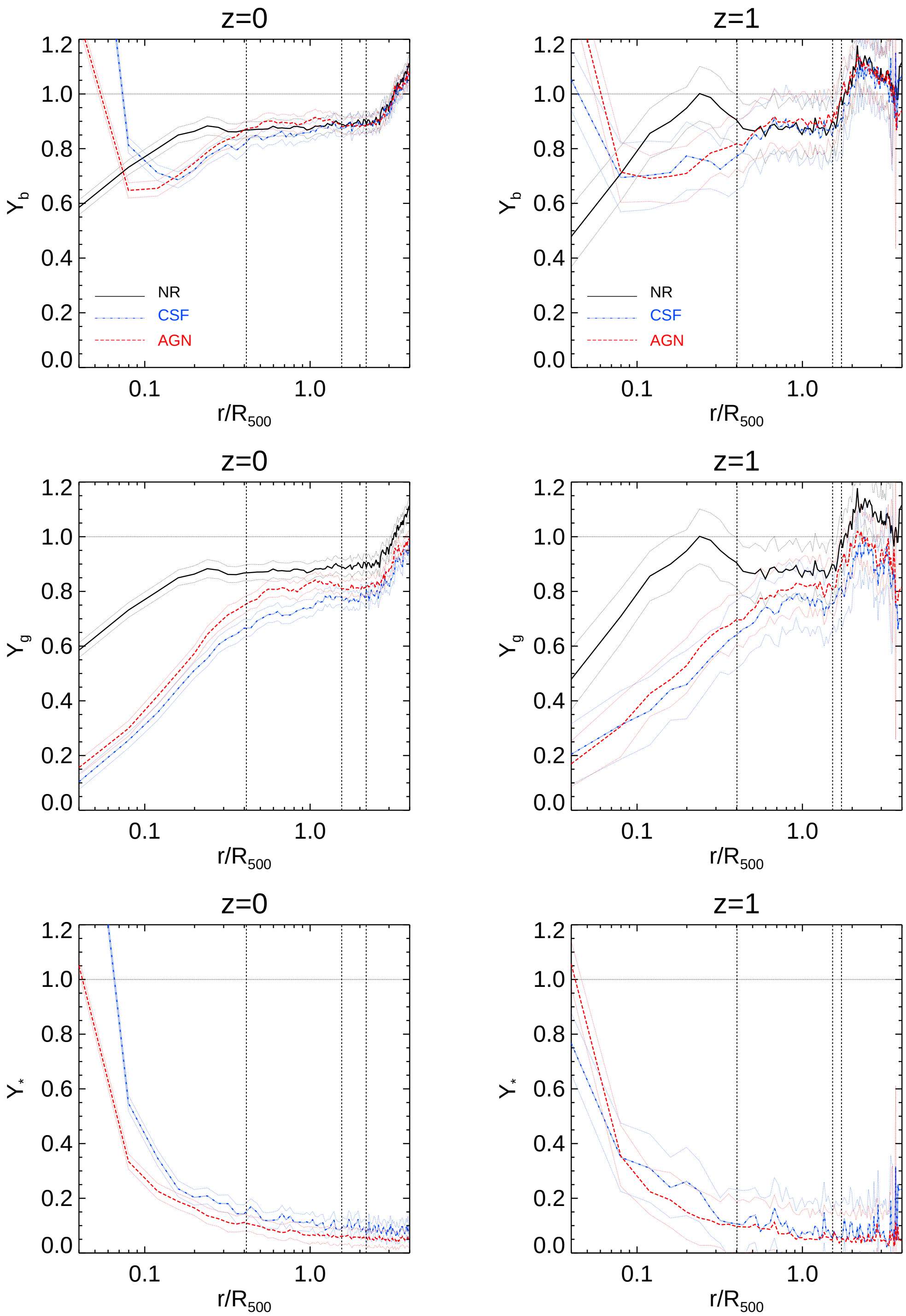

Figure 6. The mean radial profiles out to $4 \times R_{500}$ of the baryonic, gas and stellar depletions (from top to bottom panels) at $z = 0$ (left column) and $z = 1$ (right column) for the subsample of massive clusters with $M_{500} > 2 \times 10^{14}\, h^{-1} M_{\odot}$. In each panel, mean profiles for the `NR`, `CSF` and `AGN` simulated clusters are shown with the continuous black, dashed-dot blue, and long-dashed red lines, respectively. For each model, dotted lines around the mean profiles indicate the region corresponding to 1σ standard deviation around the mean. Within each panel and from left to right, dotted vertical lines indicate the position of the mean value of R_{2500}, R_{200} and R_{vir} (in units of R_{500}) for the sample of clusters for which the profiles are computed.

with the weights of the data points reported in Table 2 provided by their corresponding intrinsic scatter.

In Table 3 we report the best–fitting values of these parameters obtained for each simulation set, within different radii of interest, from R_{2500} out to the virial radius R_{vir}.

The results displayed in Fig. 8 show that, independently of the considered radius or physics, the baryon depletion factor does not evolve significantly with redshift, at least since $z = 1$. Within R_{2500} (right panel) the dissipative action of radiative cooling in the `CSF` runs slightly increases the average value of Y_b with respect to

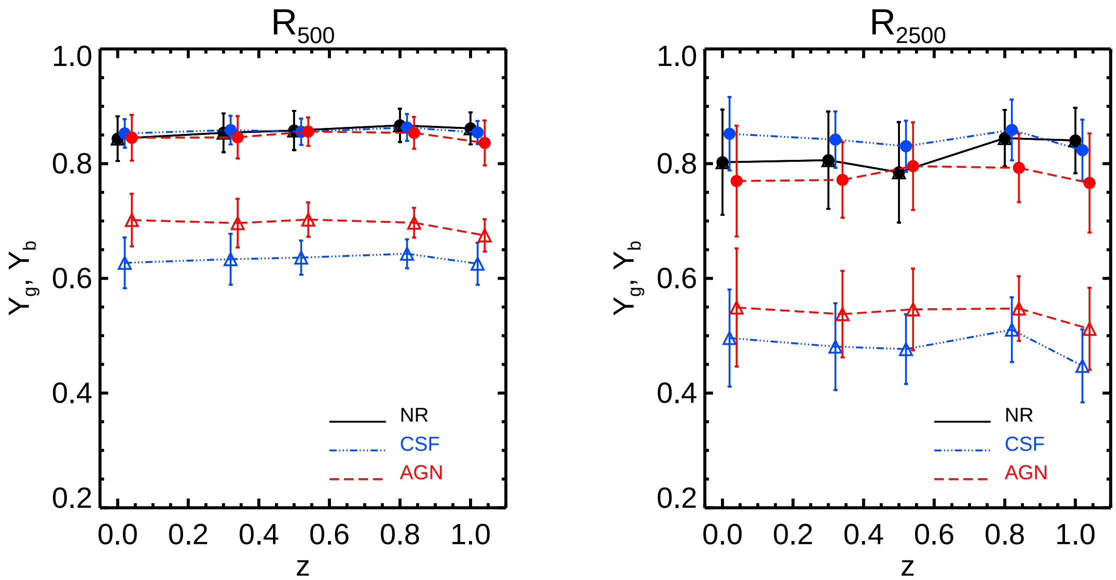

Figure 8. The redshift dependence of the mean values of gas depletion Y_g (triangles) and baryon depletion Y_b (circles), computed at R_{500} (left panel) and R_{2500} (right panel), for all clusters that at each redshift have mass $M_{500} > 2 \times 10^{14}\, h^{-1} M_\odot$. In each panel, continuous black, dashed-dot blue, and long-dashed red lines stand for the NR, CSF, and AGN simulation sets, respectively. These lines have been slightly displaced along the x-axis to avoid overlapping among them. Error bars represent 1σ intrinsic scatter computed over all simulated clusters.

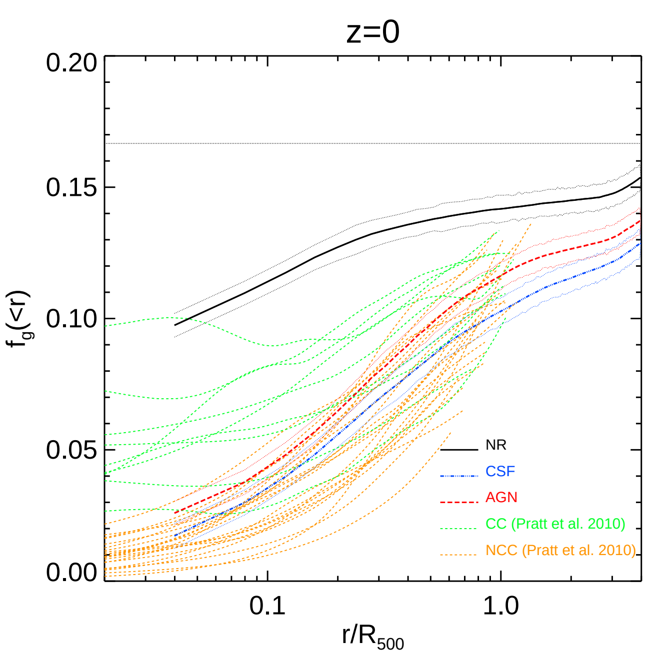

Figure 7. Comparison at $z = 0$ between the cumulative gas mass fraction profiles, $f_g(< r)$, for the clusters within each of the physical schemes adopted in our simulations and the observational data from Pratt et al. (2010). The simulated radial profiles are computed out to $4 \times R_{500}$ for the subsample of massive clusters with $M_{500} > 2 \times 10^{14}\, h^{-1} M_\odot$. Profiles for the NR, CSF and AGN simulations are shown with the continuous black, dashed-dot blue, and long-dashed red lines, respectively. For each model, dotted lines around the mean profiles indicate the region corresponding to 1σ standard deviation around the mean. Dashed lines in orange and green stand for the sample of NCC and CC systems from Pratt et al. (2010). The horizontal dotted line marks the cosmic value of the baryon mass fraction assumed in our simulations.

the AGN simulations, bringing it very close or even above to that of the non–radiative simulations, with $Y_b \simeq 0.85$, constant across the considered redshift range. On the other hand, the presence of AGN feedback is effective in preventing gas from accreting onto the central regions, thus decreasing the baryons fraction to $Y_b \simeq 0.80$, also independent of redshift.

As for results at R_{500}, we find a smaller scatter and much better agreement among the different physical models, thus highlighting that the different physical descriptions of the ICM have a negligible impact on the total amount of baryons at such larger cluster–centric radii. At such radii, we find $Y_b \simeq 0.85$ virtually independent of redshift, with some departure for the AGN simulations at $z = 1$, probably due to the limited statistics of massive clusters at the highest considered redshift. Therefore, a sizeable decrease in the baryon fraction when moving inwards to R_{2500} is detected when including the more realistic feedback scheme based on the effect of AGN.

As for the gas mass fraction, the inclusion of radiative physics decreases its value with respect to the non–radiative simulations, both at R_{2500} and at R_{500}. As expected, this decrease is more pronounced at smaller radii and for the simulations only including the effect of SN feedback. As for the AGN simulations, we find $Y_g \simeq 0.5$–0.6 within R_{2500}, quite independent of redshift, with a significant scatter, $\sigma_{Y_g} \simeq 0.1$, over the whole range of redshift. This value increases to $Y_g \simeq 0.6$–0.7 within R_{500}, also nearly constant in redshift, but with a reduced intrinsic scatter of $\sigma_{Y_g} \simeq 0.05$. The behaviour obtained for the CSF simulations is pretty similar but with lower values for the gas fraction: within R_{2500}, $Y_g \simeq 0.5$, whereas it is $Y_g \simeq 0.6$–0.7 at R_{500}. Quite remarkably, in all cases such values are nearly independent of redshift.

In general, our results for the NR case are in agreement with those from non-radiative simulations presented by Eke et al. (1998) and Ettori et al. (2006), both based on SPH simulations, while they are slightly, but systematically, lower by about 5 per cent than those obtained by Kravtsov et al. (2005) from AMR simulations.

Although this difference is quite small, it is still comparable to, or larger than, the difference induced by the presence of different physical processes in simulations. Although it remains to be seen whether such a difference between predictions of SPH and AMR codes persists when including radiative physics, its presence warns on the need of understanding in detail the performances of different hydrodynamical methods in the calibration of the gas mass fraction test through simulations. In general, our results on non–radiative simulations including only SN feedback are in line with those presented by other authors (e.g. Muanwong et al. 2002; Kravtsov et al. 2005; Ettori et al. 2006; Sembolini et al. 2012). However, while the comparison between results from different non–radiative simulations is relatively straightforward, when extra-physics is included the results on the distribution of the different baryonic components are sensitive not only to the nature of the feedback sources included (i.e. SNe vs. AGN), but also to the details of the numerical implementation (i.e. thermal vs. kinetic feedback, dependence of cooling rates on local gas metallicity, numerical resolution). These aspects have to be taken into account when performing such a comparison between results from different authors.

In principle, the results of our analysis can be used to set priors on the parameters which determine the amount of gas depletion within a given aperture radius and its redshift evolution, when deriving cosmological parameters from observations of the baryon fraction in massive clusters. Overall, the results presented in Fig. 8 (see also Table 3) allow us to set a rather strong prior on the parameter describing the evolution of Y_b (see Eq. 4), with $-0.02 \leqslant \alpha_{Y_b} \leqslant 0.07$, for a conservative range of variation holding both at R_{500} and R_{2500}, accounting for the difference between different physical models and for the uncertainties in the estimate of the mean associated to the measured intrinsic scatter. As for the normalization, a conservative allowed range of variation can be taken to be $Y_{0,b} = 0.81 \pm 0.06$ at R_{2500}, with a slightly larger normalization and narrower uncertainty (0.85 ± 0.03) at R_{500}.

In order to go one step further, we analyse the dependences of the gas and baryonic depletions as a function of any combination of the parameters $\{z, M, \Delta\}$ using the following expression:

$$Y_i(z) = Y_{0,i}(1 + \alpha_{Y_i} z)(M/M_0)^{\beta_{Y_i}}(\Delta/\Delta_0)^{\gamma_{Y_i}} \,, \quad (5)$$

where $M_0 = 5.0 \times 10^{14}\, h^{-1} M_\odot$, $\Delta_0 = 500$, and the subscript i stands for b or g when referring to the baryon or gas depletions, respectively. To obtain the values of the different parameters [$Y_{0,i}$, α_{Y_i}, β_{Y_i}, γ_{Y_i}], the least-squares fit has been performed with the IDL routine MPFIT (Markwardt 2008). For each fit we have also considered the case in which α_{Y_i} is fixed to 0, i.e., no evolution. In Table 4 we report the best–fitting values of these parameters obtained for each simulation set. In order to obtain these dependences we have considered the baryon content of our sample of massive clusters for $\Delta = 2500, 500, 200$.

In general, we note that no significant dependences upon $\{z, M, \Delta\}$ are detected. All the fitted parameters for $[\alpha_{Y_i}, \beta_{Y_i}]$ have values $\leqslant 0.07$, whereas γ_{Y_i} is in the range $[0.0, -0.04]$ for Y_b and $[0.0, -0.13]$ for Y_g.

5 SUMMARY AND DISCUSSION

In the present study, we have analysed a set of cosmological hydrodynamical simulations of galaxy clusters paying special attention to the effects that different implementations of the baryonic physics have on the baryon content of these systems. Using the newest version of the parallel Tree–PM SPH code `GADGET-3` (Springel 2005), we carried out re-simulations of 29 Lagrangian regions extracted around as many galaxy clusters identified within a low–resolution N-body parent simulation. These cluster re-simulations have been performed using different prescriptions for the baryonic physics: without including any radiative processes (`NR` runs), including the effect of cooling, star formation, SN feedback (`CSF` runs), and including also an additional contribution from AGN feedback (`AGN` runs).

The final sample of objects obtained within each one of these set of re-simulations consists in $\simeq 160$ galaxy clusters and groups with $M_{vir} \geqslant 3 \times 10^{13}\, h^{-1} M_\odot$ at $z = 0$. Using these three sets of simulated galaxy clusters, we have analysed how the different physical conditions within them affect their baryon, gas and stellar mass fractions and how these results compare with observations. We have also examined which are the implications of our results on the systematics that affect the constraints on the cosmological parameters obtained through the evolution of the cluster baryon mass fraction. In order to do so we have calibrated the different baryonic depletion factors and we have analysed their dependences on redshift, baryon physics, and cluster radius.

Our main results can be summarised as follows.

- In the `NR` simulations the baryon mass fractions within R_{500} appear flat as a function of the total mass and differ by less than ~ 10 per cent from the assumed cosmic baryon fraction. This result is consistent with previous non-radiative simulations (e.g., Eke et al. 1998; Kravtsov et al. 2005; Ettori et al. 2006). Whereas the `CSF` simulations present a similar behaviour, when AGN feedback is included there is a significant baryon depletion in poor clusters and groups, whereas the cosmic value holds only for the most massive clusters. This result, which is in agreement with the trend displayed by the observational samples from Lin et al. (2003), Giodini et al. (2009), and Laganá et al. (2011), highlights the efficiency of the AGN heating in displacing large amounts of gas outside the potential wells of small clusters and groups.
- The stellar mass fractions obtained in our radiative runs, both `CSF` and `AGN`, decreases smoothly with increasing cluster mass and shows a flattening in the low-mass end ($\leqslant 10^{14} M_\odot$) of our sample. When comparing with observational data, the obtained stellar mass fractions in our `CSF` runs is quite large, especially for massive clusters (e.g. Lin et al. 2003; Gonzalez et al. 2007; Laganá et al. 2011). When AGN feedback is included, the stellar mass fractions within R_{500} are lowered by about one third, thus alleviating the tension with observations, especially at the scale of intermediate-mass clusters. However, the level of agreement with observations depends on the observational sample we compare with. Whereas none of our runs is able to reproduce the observed strong trend of the stellar mass fraction with cluster mass reported by Gonzalez et al. (2007), our results for the AGN runs are in closer agreement with other observational samples (e.g., Laganá et al. 2011).
- When analysing the different stellar components separately, we find that the fraction of stars within R_{500} found in the BCG+ICL components is, in the `CSF` runs, of about 60 per cent for massive clusters, and of about 90 per cent for groups. Paradoxically, when AGN feedback is included we find a slightly larger fraction of stars in the BCG+ICL component. The reason for this is that, although the stellar mass of the BCG+ICL components decreases, the total stellar mass decreases more strongly. This result, in agreement with the AGN simulations by Puchwein et al. (2010), is due to the combination of two different effects: while the AGN heating truncates the star formation at high redshift, mergers keep taking place and unbinding stars from galaxies into the diffuse com-

ponent, then resulting in a net increase of the fraction of stars that end up in the ICL component.

As for the comparison with observational data, our results confirm a decreasing trend with cluster mass of the fraction of stars contributed by BCG and ICL, although they predict values of this fraction that are larger than those reported by Gonzalez et al. (2007), especially for massive clusters.

• Both of our radiative simulations show that the gas mass fraction within clusters increases with increasing cluster mass, (see also Kravtsov et al. 2005; Fabjan et al. 2010; Puchwein et al. 2010). Our results on the values of f_g at the scale of rich and poor clusters, especially in the presence of AGN feedback, are in line with some observational data sets (e.g., Vikhlinin et al. 2006; Arnaud et al. 2007; Sun et al. 2009; Zhang et al. 2011) suggesting that low-mass systems have proportionally less gas than high-mass systems.

• The results of our analysis can be used to set priors on the parameters which determine the amount of gas depletion when deriving cosmological parameters from observations of the baryon fraction in massive clusters. The baryon depletion, $Y_{\rm b}$, regardless of the considered radius or physics, is nearly constant with redshift, at least since redshift $z = 1$. However, whereas the obtained evolution for Y_b within R_{500} is virtually independent of the physics included, it shows some dependence on such physical processes when looking into inner cluster regions (R_{2500}).

• Our results allow us to set a rather strong prior on the parameter describing the evolution of Y_b (see Eq. 4), with $-0.02 \leqslant \alpha_{Y_b} \leqslant 0.07$, for a conservative range of variation holding both at R_{500} and R_{2500}, accounting for the difference between different physical models and for the uncertainties in the estimate of the mean associated to the measured intrinsic scatter. As for the normalization, a conservative allowed range of variation can be taken to be $Y_{0,b} = 0.81 \pm 0.06$ at R_{2500}, with a slightly larger normalization and narrower uncertainty, 0.85 ± 0.03, at R_{500}.

• We have analysed the dependences of the gas and baryonic depletions as a function of any combination of redshift z, cluster mass M and overdensity Δ, according to the functional form of Eq. 5. In general, we find no significant dependences of the gas and baryonic depletions on the above quantities. However, we point out that caution must be taken when using these results for cosmological applications, given that our simulated models may not span the entire range of models allowed by our current understanding of the intra-cluster medium.

In general, our results show that the star formation in our radiative runs without AGN heating, even in the presence of rather strong galactic winds, is still too efficient, especially in small clusters and groups. The situation is significantly improved when AGN feedback is included, being able to partly prevent overcooling in central cluster regions. However, a number of discrepancies between simulated and observed baryonic mass fractions within clusters still exist, especially when comparing stellar mass fractions. Nevertheless, as already reported by other authors (e.g., Fabjan et al. 2010), we can infer from our results that a feedback source associated to gas accretion onto super-massive BHs seems to go in the right direction to conciliate simulations with observations.

Overall, even when the real picture is far more complicated, with a number of complex physical processes cooperating to make AGN feedback a self-regulated process, we point out that the AGN feedback prescription used in the present work significantly improves previous results on the baryon census within clusters and brings closer simulations and observations.

In general our results highlight that a robust calibration of the baryon bias can be defined from simulations at R_{500}, which is quite constant within the range of physical models for the ICM included in our simulations. This result does not extend at the smaller radius R_{2500}, which is the typical radius within which precise measurements for the gas mass fraction have been carried out so far for distant clusters using Chandra data (Allen et al. 2011, and references therein). While being beyond the reach of the current generation of X–ray telescopes, tracing the gas content of galaxy clusters out to large radii requires the next generation of X–ray telescopes to be characterized at the same time by a large collecting area and an excellent control of the background.

ACKNOWLEDGEMENTS

The authors would like to thank Volker Springel for making available to us the non–public version of the GADGET–3 code, Annalisa Bonafede for her help with generating the initial conditions for the simulations, Weiguang Cui for useful discussions, Gabriel Pratt for supplying us with observational data to compare with, and the referee for his/her constructive comments that helped improving the presentation of the results. Simulations have been carried out at the CINECA supercomputing Centre in Bologna, with CPU time assigned through ISCRA proposals and through an agreement with University of Trieste. SP acknowledges a fellowship from the European Commission's Framework Programme 7, through the Marie Curie Initial Training Network CosmoComp (PITN-GA-2009-238356). DF acknowledges founding from the Centre of Excellence for Space Sciences and Technologies SPACE-SI, an operation partly financed by the European Union, European Regional Development Fund and Republic of Slovenia, Ministry of Higher Education, Science and Technology. This work has been supported by the PRIN-INAF09 project "Towards an Italian Network for Computational Cosmology", by the PRIN-MIUR09 "Tracing the growth of structures in the Universe", and by the PD51 INFN grant. This work has been partially supported by *Spanish Ministerio de Ciencia e Innovación* (MICINN) (grants AYA2010-21322-C03-02 and CONSOLIDER2007-00050).

REFERENCES

Allen S.W., Schmidt R.W., Fabian A.C., 2002, MNRAS, 334, L11
Allen S.W., Schmidt R.W., Fabian A.C., Ebeling H., 2003, MNRAS, 342, 287
Allen S.W., Schmidt R.W., Ebeling H., Fabian A.C., van Speybroeck L., 2004, MNRAS, 353, 457
Allen S.W., Rapetti D.A., Schmidt R.W., Ebeling H., Morris R.G., Fabian A.C., 2008, MNRAS, 383, 879
Allen S.W., Evrard A.E., Mantz A.B., 2011, ARA&A, 49, 409
Andreon S., 2010, MNRAS, 407, 263
Arnaud M., Pointecouteau E., Pratt G.W., 2007, A&A, 474, L37
Battaglia N., Bond J.R., Pfrommer C., Sievers J.L., 2012, ArXiv e-prints
Bialek J.J., Evrard A.E., Mohr J.J., 2001, ApJ, 555, 597
Biviano A., Salucci P., 2006, A&A, 452, 75
Biviano A., Murante G., Borgani S., Diaferio A., Dolag K., Girardi M., 2006, A&A, 456, 23
Böhringer H., et al., 2007, A&A, 469, 363

Bonafede A., Dolag K., Stasyszyn F., Murante G., Borgani S., 2011, MNRAS, 418, 2234
Borgani S., et al., 2004, MNRAS, 348, 1078
Borgani S., et al., 2006, MNRAS, 367, 1641
Chabrier G., 2003, PASP, 115, 763
Crain R.A., Eke V.R., Frenk C.S., Jenkins A., McCarthy I.G., Navarro J.F., Pearce F.R., 2007, MNRAS, 377, 41
David L.P., Arnaud K.A., Forman W., Jones C., 1990, ApJ, 356, 32
De Boni C., Dolag K., Ettori S., Moscardini L., Pettorino V., Baccigalupi C., 2011, MNRAS, 415, 2758
Dolag K., Borgani S., Murante G., Springel V., 2009, MNRAS, 399, 497
Dolag K., Murante G., Borgani S., 2010, MNRAS, 405, 1544
Eke V.R., Cole S., Frenk C.S., 1996, MNRAS, 282, 263
Eke V.R., Navarro J.F., Frenk C.S., 1998, ApJ, 503, 569
Ettori S., Tozzi P., Rosati P., 2003, A&A, 398, 879
Ettori S., Dolag K., Borgani S., Murante G., 2006, MNRAS, 365, 1021
Ettori S., Morandi A., Tozzi P., Balestra I., Borgani S., Rosati P., Lovisari L., Terenziani F., 2009, A&A, 501, 61
Ettori S., et al., 2004, MNRAS, 354, 111
Evrard A.E., 1990, ApJ, 363, 349
Evrard A.E., 1997, MNRAS, 292, 289
Fabjan D., Borgani S., Tornatore L., Saro A., Murante G., Dolag K., 2010, MNRAS, 401, 1670
Ferland G.J., Korista K.T., Verner D.A., Ferguson J.W., Kingdon J.B., Verner E.M., 1998, PASP, 110, 761
Frenk C.S., et al., 1999, ApJ, 525, 554
Fritz J., et al., 2011, A&A, 526, A45
Giodini S., et al., 2009, ApJ, 703, 982
Gonzalez A.H., Zaritsky D., Zabludoff A.I., 2007, ApJ, 666, 147
Haardt F., Madau P., 2001, in D.M. Neumann, J.T.V. Tran, eds., *Clusters of Galaxies and the High Redshift Universe Observed in X-rays*
He P., Liu J., Feng L.L., Shu C.W., Fang L.Z., 2006, Physical Review Letters, 96, 051302
Kapferer W., et al., 2009, A&A, 504, 719
Kauffmann G., et al., 2003, MNRAS, 341, 33
Kay S.T., Thomas P.A., Jenkins A., Pearce F.R., 2004, MNRAS, 355, 1091
Komatsu E., et al., 2011, ApJS, 192, 18
Kravtsov A., Borgani S., 2012, ArXiv e-prints
Kravtsov A.V., Nagai D., Vikhlinin A.A., 2005, ApJ, 625, 588
Laganá T.F., Lima Neto G.B., Andrade-Santos F., Cypriano E.S., 2008, A&A, 485, 633
Laganá T.F., Zhang Y.Y., Reiprich T.H., Schneider P., 2011, ApJ, 743, 13
LaRoque S.J., Bonamente M., Carlstrom J.E., Joy M.K., Nagai D., Reese E.D., Dawson K.S., 2006, ApJ, 652, 917
Leauthaud A., et al., 2012, ApJ, 746, 95
Lin Y.T., Mohr J.J., 2004, ApJ, 617, 879
Lin Y.T., Mohr J.J., Stanford S.A., 2003, ApJ, 591, 749
Lin Y.T., Stanford S.A., Eisenhardt P.R.M., Vikhlinin A., Maughan B.J., Kravtsov A., 2012, ApJL, 745, L3
Lubin L.M., Cen R., Bahcall N.A., Ostriker J.P., 1996, ApJ, 460, 10
Markwardt C.B., 2008, in *Proc. Astronomical Data Analysis Software and Systems XVIII, Quebec, Canada, ASP Conference Series, Vol. 411, p. 251-254*
McCarthy I.G., Bower R.G., Balogh M.L., 2007, MNRAS, 377, 1457
McCarthy I.G., Schaye J., Bower R.G., Ponman T.J., Booth C.M., Dalla Vecchia C., Springel V., 2011, MNRAS, 412, 1965
Metzler C.A., Evrard A.E., 1994, ApJ, 437, 564
Mohr J.J., Mathiesen B., Evrard A.E., 1999, ApJ, 517, 627
Muanwong O., Thomas P.A., Kay S.T., Pearce F.R., 2002, MNRAS, 336, 527
Murante G., Giovalli M., Gerhard O., Arnaboldi M., Borgani S., Dolag K., 2007, MNRAS, 377, 2
Murante G., et al., 2004, ApJL, 607, L83
Nagai D., Vikhlinin A., Kravtsov A.V., 2007, ApJ, 655, 98
Navarro J.F., Frenk C.S., White S.D.M., 1995, MNRAS, 275, 720
Onions J., et al., 2012, MNRAS, 423, 1200
Padovani P., Matteucci F., 1993, ApJ, 416, 26
Pen U.L., 1997, New Astronomy, 2, 309
Pierini D., Zibetti S., Braglia F., Böhringer H., Finoguenov A., Lynam P.D., Zhang Y.Y., 2008, A&A, 483, 727
Planck Collaboration, et al., 2011, A&A, 536, A10
Pratt G.W., Croston J.H., Arnaud M., Böhringer H., 2009, A&A, 498, 361
Pratt G.W., et al., 2010, A&A, 511, A85
Puchwein E., Sijacki D., Springel V., 2008, ApJL, 687, L53
Puchwein E., Springel V., Sijacki D., Dolag K., 2010, MNRAS, 406, 936
Rudick C.S., Mihos J.C., McBride C., 2006, ApJ, 648, 936
Salpeter E.E., 1955, ApJ, 121, 161
Sasaki S., 1996, PASJ, 48, L119
Sembolini F., Yepes G., De Petris M., Gottloeber S., Lamagna L., Comis B., 2012, ArXiv e-prints
Short C.J., Thomas P.A., 2009, ApJ, 704, 915
Short C.J., Thomas P.A., Young O.E., Pearce F.R., Jenkins A., Muanwong O., 2010, MNRAS, 408, 2213
Sijacki D., Springel V., Di Matteo T., Hernquist L., 2007, MNRAS, 380, 877
Springel V., 2005, MNRAS, 364, 1105
Springel V., Hernquist L., 2003a, MNRAS, 339, 289
Springel V., Hernquist L., 2003b, MNRAS, 339, 312
Springel V., White S.D.M., Tormen G., Kauffmann G., 2001, MNRAS, 328, 726
Springel V., Di Matteo T., Hernquist L., 2005, MNRAS, 361, 776
Sun M., Voit G.M., Donahue M., Jones C., Forman W., Vikhlinin A., 2009, ApJ, 693, 1142
Sutherland R.S., Dopita M.A., 1993, ApJS, 88, 253
Tormen G., Bouchet F.R., White S.D.M., 1997, MNRAS, 286, 865
Tornatore L., Borgani S., Dolag K., Matteucci F., 2007, MNRAS, 382, 1050
Vikhlinin A., Kravtsov A., Forman W., Jones C., Markevitch M., Murray S.S., Van Speybroeck L., 2006, ApJ, 640, 691
White S.D.M., Frenk C.S., 1991, ApJ, 379, 52
White S.D.M., Navarro J.F., Evrard A.E., Frenk C.S., 1993, Nature, 366, 429
Wiersma R.P.C., Schaye J., Smith B.D., 2009, MNRAS, 393, 99
Young O.E., Thomas P.A., Short C.J., Pearce F., 2011, MNRAS, 413, 691
Zhang Y.Y., Laganá T.F., Pierini D., Puchwein E., Schneider P., Reiprich T.H., 2011, A&A, 535, A78
Zibetti S., White S.D.M., Schneider D.P., Brinkmann J., 2005, MNRAS, 358, 949

Table 1. Best–fit functional forms for the baryon (f_b), gas (f_g) and stellar (f_*) mass fractions as a function of the total cluster mass, M_{500}, for different analyses of observational data.

Sample	Best fit
Lin et al. (2003)	$f_{\rm b,500} = 0.148^{+0.005}_{-0.004}(M_{500}/[3\times10^{14}{\rm M}_\odot])^{(0.148\pm0.040)}$
Giodini et al. (2009)	$f_{\rm b,500} = (0.123\pm0.003)(M_{500}/[2\times10^{14}{\rm M}_\odot])^{(0.09\pm0.03)}$
Laganá et al. (2011)	$f_{\rm b,500} = 0.117^{+0.060}_{-0.040}(M_{500}/10^{14}{\rm M}_\odot)^{(0.136\pm0.028)}$
Z11+S09	$f_{\rm g,500} = (0.085\pm0.004)(M_{500}/[10^{14}{\rm M}_\odot])^{(0.30\pm0.07)}$
V06+APP07+S09	$f_{\rm g,500} = (0.093\pm0.002)(M_{500}/[2\times10^{14}{\rm M}_\odot])^{(0.21\pm0.03)}$
Lin et al. (2003)	$f_{*,500} = 0.0164^{+0.0010}_{-0.0090}(M_{500}/[3\times10^{14}{\rm M}_\odot])^{-(0.26\pm0.09)}$
Gonzalez et al. (2007)	$f_{*,500} = (0.009\pm0.002){M_{500}}^{-(0.64\pm0.13)}$
Laganá et al. (2011)	$f_{*,500} = 0.029^{+0.008}_{-0.006}(M_{500}/[10^{14.5}{\rm M}_\odot])^{(-0.36\pm0.17)}$

Table 2. Values of the gas, stellar and baryonic depletion factors (Y_g, Y_* and Y_b, respectively) for our set of simulated clusters, for the three different physical models (NR, CSF, and AGN), computed at R_{2500} and R_{500}. In each case, values computed at redshifts $z = 0, 0.3, 0.5, 0.8$ and 1 are reported. We show within brackets the values of the intrinsic scatters computed within the ensamble of simulated clusters. Results are shown for the subset of clusters that, at each redshift, are more massive than $M_{500} = 2\times10^{14}\,h^{-1}M_\odot$.

Simulation	z	R_{2500}			R_{500}		
		$Y_{\rm g}$	Y_*	$Y_{\rm b}$	$Y_{\rm g}$	Y_*	$Y_{\rm b}$
NR	0.0	0.80 (0.09)	–	0.80 (0.09)	0.84 (0.04)	–	0.84 (0.04)
NR	0.3	0.81 (0.08)	–	0.81 (0.08)	0.85 (0.03)	–	0.85 (0.03)
NR	0.5	0.78 (0.09)	–	0.78 (0.09)	0.86 (0.03)	–	0.86 (0.03)
NR	0.8	0.84 (0.05)	–	0.84 (0.05)	0.87 (0.03)	–	0.87 (0.03)
NR	1.0	0.84 (0.06)	–	0.84 (0.06)	0.86 (0.03)	–	0.86 (0.03)
CSF	0.0	0.49 (0.08)	0.34 (0.07)	0.85 (0.06)	0.63 (0.04)	0.21 (0.04)	0.85 (0.02)
CSF	0.3	0.48 (0.08)	0.34 (0.06)	0.84 (0.05)	0.63 (0.04)	0.21 (0.03)	0.86 (0.03)
CSF	0.5	0.48 (0.06)	0.32 (0.05)	0.83 (0.04)	0.64 (0.03)	0.20 (0.02)	0.86 (0.02)
CSF	0.8	0.51 (0.06)	0.31 (0.05)	0.86 (0.05)	0.64 (0.03)	0.19 (0.02)	0.86 (0.02)
CSF	1.0	0.45 (0.06)	0.33 (0.06)	0.82 (0.05)	0.63 (0.04)	0.19 (0.03)	0.85 (0.02)
AGN	0.0	0.55 (0.10)	0.21 (0.03)	0.77 (0.09)	0.70 (0.05)	0.13 (0.02)	0.85 (0.04)
AGN	0.3	0.54 (0.08)	0.21 (0.04)	0.77 (0.07)	0.70 (0.04)	0.13 (0.02)	0.85 (0.04)
AGN	0.5	0.55 (0.07)	0.22 (0.04)	0.80 (0.08)	0.70 (0.03)	0.13 (0.01)	0.86 (0.02)
AGN	0.8	0.55 (0.06)	0.21 (0.02)	0.79 (0.06)	0.70 (0.03)	0.13 (0.01)	0.85 (0.03)
AGN	1.0	0.51 (0.07)	0.21 (0.05)	0.77 (0.09)	0.68 (0.03)	0.13 (0.02)	0.84 (0.04)

Table 3. Best–fit values of the parameters describing the evolution of the gas and baryonic depletions, according to Eq. 4. For each simulation set (NR, CSF, and AGN) and radius of interest (R_{2500}, R_{500}, R_{200}, and R_{vir}), we show the normalization ($Y_{0,i}$) and slope (α_{Y_i}) of the relation, along with their respective standard deviations within brackets, as obtained from the χ^2 minimization procedure.

Simulation	Radius	$Y_{0,g}$	α_{Y_g}	$Y_{0,b}$	α_{Y_b}
NR	R_{vir}	0.87 (0.02)	0.00 (0.04)	0.87 (0.02)	0.00 (0.04)
NR	R_{200}	0.86 (0.02)	0.00 (0.04)	0.86 (0.02)	0.00 (0.04)
NR	R_{500}	0.85 (0.03)	0.02 (0.05)	0.85 (0.03)	0.02 (0.05)
NR	R_{2500}	0.79 (0.07)	0.07 (0.12)	0.79 (0.07)	0.07 (0.12)
CSF	R_{vir}	0.70 (0.03)	-0.03 (0.06)	0.87 (0.02)	-0.01 (0.03)
CSF	R_{200}	0.68 (0.03)	0.00 (0.06)	0.86 (0.02)	-0.01 (0.03)
CSF	R_{500}	0.63 (0.03)	0.01 (0.08)	0.86 (0.02)	0.00 (0.03)
CSF	R_{2500}	0.49 (0.06)	-0.04 (0.18)	0.85 (0.05)	-0.02 (0.08)
AGN	R_{vir}	0.76 (0.03)	-0.04 (0.05)	0.87 (0.02)	-0.01 (0.04)
AGN	R_{200}	0.75 (0.03)	-0.03 (0.05)	0.87 (0.03)	-0.01 (0.04)
AGN	R_{500}	0.71 (0.03)	-0.03 (0.06)	0.85 (0.03)	0.00 (0.05)
AGN	R_{2500}	0.55 (0.07)	-0.04 (0.18)	0.78 (0.07)	0.01 (0.14)

Table 4. Best–fit values of the parameters describing the evolution of the gas and baryonic depletions according to Eq. 5. For each simulation set (`NR`, `CSF`, and `AGN`) and using the data within different radii of interest (R_{2500}, R_{500} and R_{200}), we show the best-fit values for the different parameters describing all the dependences of the gas and baryonic depletions ($Y_{0,i}$, α_{Y_i}, β_{Y_i}, γ_{Y_i}), along with their respective uncertainties within brackets. The quoted uncertainties on the best-fit parameters are obtained from the un-weighted least-squares fit rescaled by $(\chi^2/\mathrm{DOF})^{1/2}$ under the assumption that the value of the true reduced χ^2 is unity. For each fit we have also considered the case in which there is no redshift evolution, i.e., α_{Y_i} is fixed to 0. This case is shown in the second row for each simulation.

Simulation	$Y_{0,g}$	α_{Y_g}	β_{Y_g}	γ_{Y_g}	$Y_{0,b}$	α_{Y_b}	β_{Y_b}	γ_{Y_b}
`NR`	0.84 (0.01)	0.03 (0.01)	0.01 (0.01)	-0.03 (0.01)	0.84 (0.01)	0.03 (0.01)	0.01 (0.01)	-0.03 (0.01)
`NR`	0.84 (0.01)	0.00	0.00 (0.01)	-0.03 (0.01)	0.84 (0.01)	0.00	0.00 (0.01)	-0.03 (0.01)
`CSF`	0.60 (0.01)	0.06 (0.02)	0.07 (0.01)	-0.13 (0.01)	0.85 (0.01)	0.00 (0.01)	0.01 (0.01)	-0.01 (0.01)
`CSF`	0.61 (0.01)	0.00	0.05 (0.01)	-0.13 (0.01)	0.85 (0.01)	0.00	0.01 (0.01)	-0.01 (0.01)
`AGN`	0.67 (0.01)	0.02 (0.02)	0.06 (0.01)	-0.12 (0.01)	0.83 (0.01)	0.03 (0.01)	0.03 (0.01)	-0.04 (0.01)
`AGN`	0.68 (0.01)	0.00	0.06 (0.01)	-0.12 (0.01)	0.84 (0.01)	0.00	0.03 (0.01)	-0.04 (0.01)